Opto-Electronics Review 28 (2020) 93-98

PAN POLISH ACADEMY OF SCIENCES

Opto-Electronics Review

journal homepage: http://journals.pan.pl/opelre

A new design of scanning IR detectors

S.A. Dvoretsky[a], A.P. Kovchavtsev[a], I.I. Lee[a]*, V.G. Polovinkin[a,b], G.Yu. Sidorov[a], M.V. Yakushev[a]

[a] Rzhanov Institute of Semiconductor Physics, 13 Acad. Lavrentiev Ave., 630090 Novosibirsk, Russian Federation.
[b] Novosibirsk State Technical University, 20 Marx Ave., 630073 Novosibirsk, Russian Federation.

Article info

Article history:
Received 12 Mar 2020
Received in revised form 13 May 2020
Accepted 14 May 2020

Keywords:
scanning IR detector, photosensitive element, Monte Carlo method, local quantum efficiency, point radiation source.

Abstract

Photoelectrical characteristics of scanning IR detectors with implemented time delay and integration mode are analyzed. A new "shifted cellular" layout of photosensitive elements in the FPA structure is proposed. Advantages of the new FPA configuration in terms of threshold sensitivity for small-size/point objects are demonstrated. The analysis is based on the Monte Carlo simulation of the diffusion process of photogenerated minority charge carriers in the photosensitive layer photodiode arrays. The analysis is performed taking into account the main photoelectric parameters of FPA elements: photosensitive layer thickness, diffusion length of charge carriers, optical absorption length, their design parameters: geometric sizes of FPA elements, diameters of *p-n* junctions, and design parameters of the optical system: optical-spot diameter.

1. Introduction

In the early 90s Sofradir (France) developed 4×288 PLUTON LW linear infrared focal plane array (IR FPA) intended for operation in time delay and integration (TDI) mode [1]. That FPA included two 4×144 identical photodiode sub-arrays, each having a sparse pixel layout with a 56-μm pitch. For making the FPA structure continuous, the second identical sub-array was shifted by one-half of the FPA pitch, thus yielding a 28 μm pitch size [1,2]. The implemented FPA structure was proposed considering the available technological possibilities in manufacturing Si readout integrated circuits. Numerous modifications of the 4×288 PLUTON LW FPA aiming at increasing sensitivity and spatial resolution of photodetectors were developed, achieved mainly by improving the silicon readout integrated circuit and the manufacturing technology of detectors, scanning system, and video imaging software. The microscanning in two directions, performed with a step smaller than the FPA pitch, has made it possible to register 576×768 thermal images [2]. The experience gained in using such IR FPAs has predetermined the design of subsequent scanning IR FPAs [3,4].

With the present-day technological capabilities, technical solutions adopted in the discussed IR FPA cannot be considered optimal; yet, the scanning linear IR FPAs are still called in systems where it is required to measure multispectral images with a spatial resolution that cannot be achieved using staring IR FPAs [4,5].

The purpose of the present study was a development of an advanced design of scanning linear IR FPAs ensuring increased sensitivity and spatial resolution of IR FPA detectors, and reducing their cost, weight, and size.

2. Photoelectrical characteristics of FPA elements on MCT layers

Numerical models of FPAs for calculating their photoelectrical characteristics were developed either on the basis of the direct solution of a diffusion equation [6,7] or using the Monte Carlo approach for modeling of a diffusion process of photogenerated charge carriers [8,9]. The FPA model used in the present study was based on the Monte Carlo analysis of a 3D diffusion process of photogenerated charge carriers in a photosensitive layer of multi-element FPAs on HgCdTe; this model was described in Refs. 10 - 12. A distinguishing feature of the model is the preliminary calculation of a local quantum efficiency a real distribution. It is allowing one to rapidly calculate levels of pixel signals by convolving distribution of a local

* Corresponding author e-mail irlamlee@isp.nsc.ru

https://doi.org/10.24425/opelre.2020.132505

quantum efficiency of FPA element with an arbitrary optical image, for instance, an optical spot due to a point radiation source.

Figure 1 shows the calculated integral-quantum-efficiency dependences i.e. signal produced by photosensitive element (PE) *vs.* the photosensitive layer thickness (T_{PL}) for a uniform illumination of FPA in the planar version of PLUTON LW topology with pixel sizes of 56×56 μm [Fig. 1(a)] and 28×28 μm [Fig. 1(b)]. The calculations were performed assuming values of the charge-carrier diffusion length (L_D) and the optical absorption length (L_{Opt}) being typical of MBE-grown HgCdTe layers [13]. For the diameter of the *p-n* junctions (D_{pn}), the value of 14 μm was adopted [12]. Under quantum efficiency, we understand the amount of photodiode-collected photogenerated charge carriers normalized by the amount of photons having fallen onto illuminated FPA element. Light reflections from the photosensitive layer (PL) boundaries were ignored.

Figure 2 shows the calculated curves of the integral quantum efficiency of FPA elements under local illumination within the border of the central FPA element sub-arrays. Note the significant difference in the curves of quantum efficiency for the cases of uniform and local illumination of sparsely and closely spaced FPAs.

Under local illumination, the quantum efficiency is noticeably smaller than that under uniform illumination of the entire FPA. Under uniform illumination, the diffusion flux of photogenerated charge carriers from the central FPA element into neighboring photovoltaic cells is compensated by the opposite flux of photogenerated carriers from the neighboring photovoltaic cells; under local illumination, no such compensation occurs. For the sparse layout of FPA photodiodes, the quantum efficiency in both cases, of uniform and local illumination, decreases significantly, while the effect due to L_{Opt} and L_D becomes more pronounced, even if the length L_D varies in a rather narrow range of 15 to 25 μm.

When planar technology is used, the spacing between *p-n* photodiodes should be made significantly smaller than the diffusion length of minority charge carriers. With a sparse layout of FPA elements in the FPA structure and with a step 56 μm FPA pitch, this condition is not satisfied. It leads to a decrease in quantum efficiency and a pronounced scatter of Volt/Watt characteristics of FPA elements, due to the recombination of a significant fraction

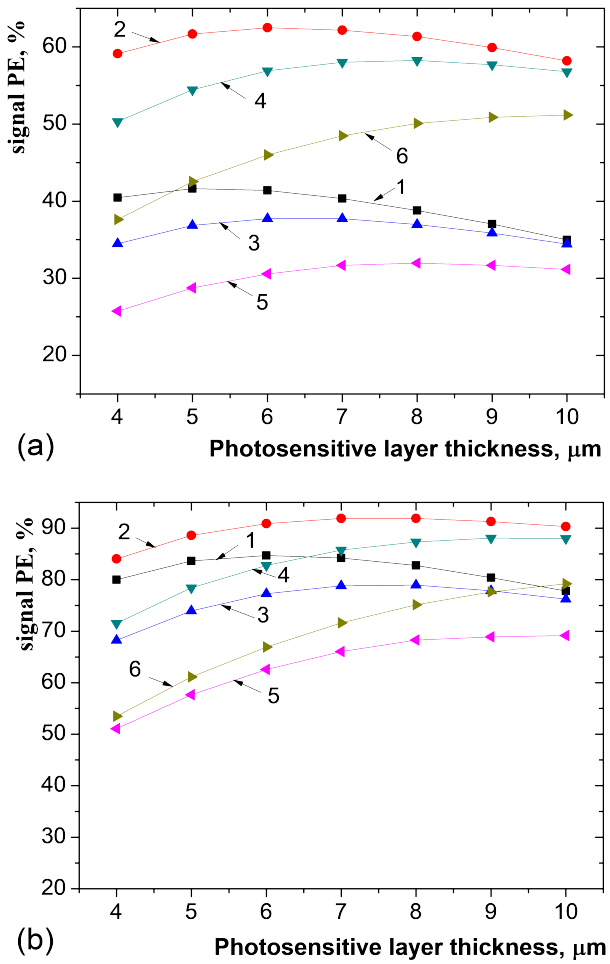

Fig. 1. The integral quantum efficiency of PEs sized of 56×56 μm [Fig. 1(a)] and 28×28 μm [Fig. 1(b)] under uniform illumination of the entire FPA *vs.* TPL. L_D: 15 μm (curves 1, 3, and 5), 25 μm (curves 2, 4, and 6); L_{Opt}: 2 μm (curves 1 and 2), 3 μm (curves 3 and 4), 5 μm (curves 5 and 6).

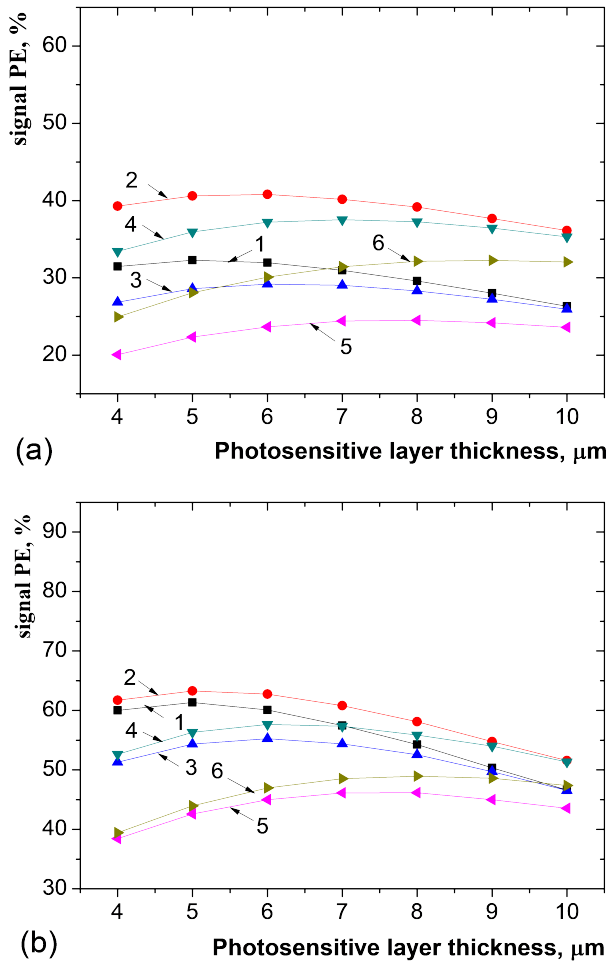

Fig. 2. The integral quantum efficiency of PEs sized of 56×56 μm [Fig. 2(a)] and 28×28 μm [Fig. 2(b)] under their local illumination *vs.* the absorber thickness. Diffusion length of minority charge carriers L_D: 15 μm (curves 1, 3, and 5), 25 μm (curves 2, 4, and 6); optical absorption length L_{Opt}: 2 μm (curves 1 and 2), 3 μm (curves 3 and 4), 5 μm (curves 5 and 6).

of photogenerated charge carriers in the photosensitive layer. Similar calculations performed for an FPA with 20×20 μm pixel size were previously reported in Ref. 11. Therefore, for a linear scanning IR FPA of the PLUTON LW type, with a sparsely arrangement of FPA elements with a step of 56 μm, the suppression of photosensitivity outside the central region of 28×28 μm FPA elements (for the PLUTON LW FPA) is in essentially required. For this purpose, either the isolation of *p-n* junctions with *p-n* guard junctions, which restrict the collection area of FPA elements [1], or more sophisticated technologies [1], such as, e.g., mesa-technology or using metallized masks for shielding pixel boundaries [9] can be used. However, the use of optical shielding technology leads to considerable losses of optical signals in the focal plane of IR detectors (~ 75%) and, hence, to the decreased sensitivity.

3. Architecture of future linear photodiode sub-arrays for IR FPA detectors

The modern technologies for fabrication of FPAs and Si readout integrated circuits permit the reduction of pixel sizes and the use of topological solutions with close packing of PEs in linear TDI IR FPAs.

One of the main functions of linear scanning multi-element IR FPAs is detection and identification of small-sized or point objects [14,15]. We assume the radiation intensity in the optical spot due to a point radiation source in the focal plane of IR FPA to be a result of Fraunhofer diffraction on a round hole. Here, the spot diameter (D_{Opt}) is a diameter of the first dark circle, inside which ~ 84% of the total energy of the optical spot is concentrated [16].

Tables 1 and 2 list levels of optical signals falling onto an FPA element and levels of the photoelectrical signals produced by 20×20 and 5×5 μm PEs (normalized by the number of photons in the optical spot, D_{Opt} =20 μm, in %) *vs*. the position of the spot center relative to the center of the FPA element. This value characterizes the quantum efficiency of FPA elements for small-sized point radiation sources. The values of D_{pn}, L_{Opt}, and L_D used in the calculations are indicated in the tables.

Among the above results, we would like to note the increase in the ratio between the levels of optical signals and photoelectric signals produced by the FPA elements with the reducing pixel size. This increase is due to a decrease of local quantum efficiency observed on decreasing the pixel size. The levels of the optical signals and those of the signals produced by FPA elements will be identical for an "ideal" FPA in which the local quantum efficiency of each FPA element is unity inside the area occupied by the FPA element and zero outside this area. A disadvantageous feature of the traditional layout of FPA elements in registering point objects is rather a strong dependence of the signal levels on the position of the spot center relative to the FPA element center. Probability of identification of a point radiation source is defined by the minimum signal level, observed when the center of the optical spot is located among four pixels (the third column in Tables 1 and 2). The fourth and fifth columns show the signal levels for the cases in which the center of the optical spot is projected at the center of a neighboring or diagonally located FPA element; those signal levels characterize the inter-pixel crosstalk values.

Table 1

FPA parameters and signal level due to a point radiation source at different locations of the optical-spot center, for traditional topology.

FPA parameters		Signal level				
Pixel size 20×20 μm	L_{Opt} μm	At the center of the pixel	Inbetween two pixels.	Among four pixels	At the center of neigh-bouring pixels	At the center of diagonal pixels
L_D= 20 μm T_{PL}= 5 μm D_{pn}=10 μm	2 5	66.61 46.73	31.69 22.03	18.52 12.75	3.3 2.05	1.01 0.67
L_D =20 μm T_{PL} = 5 μm D_{pn}=16 μm	2 5	73.72 51.45	37.62 26.08	20.49 14.13	2.4 1.55	0.69 0.46
The fraction of photons in the optical spot falling onto pixel, (%)		84.47	43.89	23.08	2.03	0.58

Table 2

FPA parameters and signal level due to a point radiation source at different locations of the optical-spot center, for traditional topology.

FPA parameters		Signal level				
Pixel size 5×5 μm	L_{Opt} μm	At the center of the pixel	Inbetween two pixels.	Among four pixels	At the center of neigh-bouring pixels	At the center of diagonal pixels
L_D =15 μm T_{PL}= 4 μm D_{pn}= 3 μm	2 5	14.46 9.69	12.29 8.19	10.44 6.91	7.50 4.88	3.89 2.44
L_D =25 μm T_{PL} = 4 μm D_{pn} = 3 μm	2 5	14.58 9.75	12.41 8.25	10.54 6.96	7.59 4.94	3.95 2.49
The fraction of photons in the optical spot falling onto pixel, (%)		25.05	20.33	16.41	10.45	3.86

The "shifted cellular" FPA configuration shown in Fig. 3 reduces dependence of signal levels on the position of the optical spot relative to the pixel center.

In contrast to the case of traditional FPAs, each second FPA line in the shown FPA is shifted relative to either of its neighbor lines by one-half of the pitch, i.e. a/2.

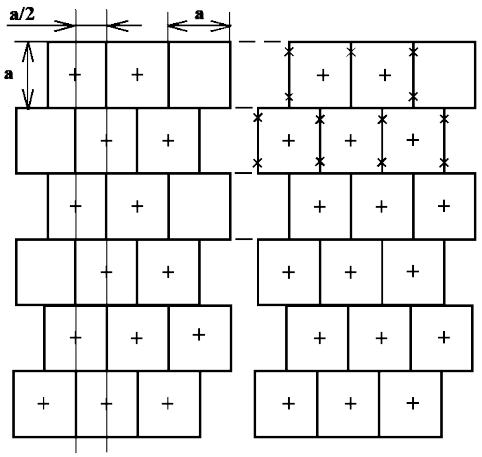

Fig. 3. The "shifted cellular" layout of FPA elements in FPA structure.

Table 3 lists the signal levels for the central FPA element *vs.* photoelectric and design parameters of the "shifted cellular" FPA configuration for various locations of the optical-spot center relative to the FPA element center. The adopted values of absorber thickness, optical absorption length, diameters of *p-n* junctions, and charge-carrier diffusion length are the same as those in Table 1.

Table 3

FPA parameters and signal level due to a point radiation source at different locations of the optical-spot center, for traditional topology. The signal is integrated by the central FPA element, for "the shifted cellular" topology.

FPA parameters		Signal level			
Pixel size 5x5 μm	L_{Opt} μm	At the center of the pixel	Minimum level (at the point **x**).	At the center of neigh-bouring pixels	At the center of diagonal pixels
L_D = 20 μm T_{PL} = 5 μm D_{pn} = 10 μm	2 5	66.85 46.94	23.14 15.97	3.23 2.09	1.23 0.84
L_D = 20 μm T_{PL} = 5 μm D_{pn} = 16 μm	2 5	73.99 51.7	26.57 18.4	2.36 1.55	0.66 0.44
The fraction of photons in the optical spot falling onto pixel, (%)		84.45	34.93	2.07	0.58

A minimum signal level for the "shifted cellular" FPA is achieved when the center of the optical spot is located at the points **x** (see Fig 3 and Table 3, the third column). For the photo signals produced by PEs, the coordinates of the point x relatively weakly depend on the photoelectrical characteristics of PEs. For example for PEs with 20×20 μm pixel size at D_{Opt} = 20 μm the distance from the point x to the center of the FPA cell varies, depending on the photoelectrical parameters of FPA (PL thickness, L_D, and L_{opt}), in the range from 7.28 to 7.4 μm.

Comparison of Tables 1 and 3 shows that, at all other conditions being identical, the minimum signal levels due to point radiation sources for the "shifted cellular" FPA configuration exceed the minimum signal levels for an FPA with the traditional layout of FPA elements. Therefore, for small-size/point objects the "shifted cellular" topology of FPA elements will ensure a better threshold sensitivity. The some identical of FPA lines allows using the TDI mode, whereas the shift of every second line by one-half of the pitch, an increase spatial resolution, in a single-array design. The design of the scanner is now simplified, since the sub-scanning by one-half of the pitch along the linear FPA becomes unnecessary.

In Fig. 4 are the calculations the levels of optical signals [Fig. 4(a)] and the levels of the signals produced by PEs of traditional configuration [Fig. 4(b)] (%, the fraction of photons of a full number of photons in the optical spot, and on the assumption that the number of photons in the optical spot does not depend on the spot diameter) *vs.* on pixels sized and the location of the center of the optical spot in relation to the center of PE. The design parameters (D_{pn} and T_{PL}) for each pixel size were chosen from preliminary calculations performed to ensure a maximum integral quantum efficiency. For the 5×5 μm FPA cell, the adopted values are T_{PL} = 4 μm and D_{pn} = 3 μm, whereas for the 8×8, 10×10, 12×12, 15×15, and 20×20 μm FPA cells, we assumed that T_{PL} = 5 μm; D_{pn} = 4, 6, 8, 10, and 16 μm, respectively; L_D = 20 μm, L_{Opt} = 3 μm.

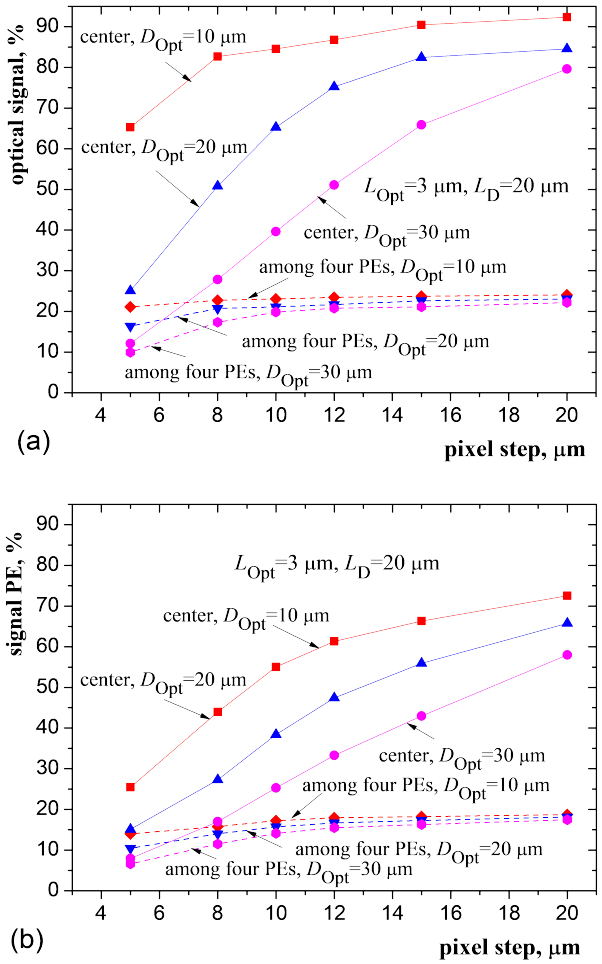

Fig. 4. The optical signals (a) and the PE signals (b) *vs.* the pixel size for point radiation sources producing optical spots 10, 20, and 30 μm in diameter (%, the fraction of photons of a full number of photons in the optical spot).

Dependences of the signal levels due to a point radiation source allow us to calculate the threshold sensitivity of the IR FPA under uniform illumination and also, for small-size/point objects. Suppose that IR FPA has sensitivity close to BLIP mode. The threshold sensitivity for point radiation sources and that under uniform illumination of FPA is given by the following modified expression [17]:

$$NEP(\lambda, T_{int}) = \frac{1}{\eta_s}\left[\frac{\eta_{ui} Q_{bg} A_{det}}{T_{int}}\right]^{\frac{1}{2}}\left[\frac{hc}{\lambda}\right]. \qquad (1)$$

Here, η_s - signals level from a PE (the fraction of photons of a full number of photons in a spot, in %) for a chosen optical spot diameter and optical spot position relative to the PE center; η_{ui} - quantum efficiency under uniform illumination; Q_{bg} - background radiation density in photons/sec; A_{det} - PE area; T_{int} - integration time; h - Planck constant and λ - light wavelength.

We assume that for an FPA element sized 5×5 μm, at an arbitrary background radiation level and the spectral range the threshold sensitivity in relative units is 1.

Under such conditions Fig. 5 shows the calculated dependences of the threshold sensitivity in relative units on the size of PE. These dependences were calculated taking into account the local distribution of quantum efficiency under uniform illumination of FPA and for point radiation sources with D_{Opt} 10, 20, and 30 μm.

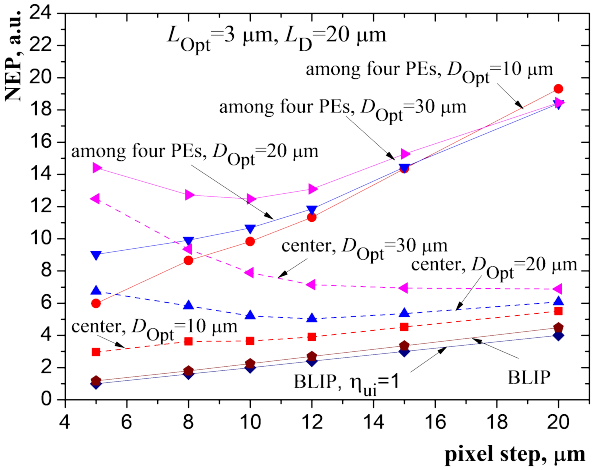

Fig. 5. The dependence of NEP on the pixel size in an IR FPA operating in BLIP mode and used for L_{opt} - 10, 20, and 30 μm at two locations of the spot center relative to the measuring FPA element. The spot center is projected onto the FPA plane at the center of the FPA element and in between the four neighboring FPA elements in a traditional FPA.

In this Figure there are also the limit NEP values in the BLIP mode for PE at $\eta_{ui} = 1$, ("BLIP, $\eta_{ui} = 1$" curve), and the NEP values for PEs with the quantum efficiency dependences on PE sizes under the uniform illumination ("BLIP" curve). Thereat, it is necessary to take into account that the calculated quantum efficiency values mentioned in the present contribution do not consider optical signal losses in real devices, in particular, reflection from a nonplanar PE surface, etc.

In the case in which the spot center is projected into the center of the FPA element, the levels of the optical signals due to a point radiation source, the levels of the signals generated by the PEs and, accordingly, the threshold sensitivity are all almost independent of the FPA configuration (traditional or "shifted cellular"). Figure 6 shows the calculated dependences of the threshold sensitivity of IR FPA for the worst-case position of the center of the optical spot for the traditional FPA configuration (the spot center is in between four FPA elements) and for the "shifted cellular" FPA configuration (the spot center is at the point x in Fig. 3). The dependences shown in Fig. 6 prove that the "shifted cellular" FPA configuration

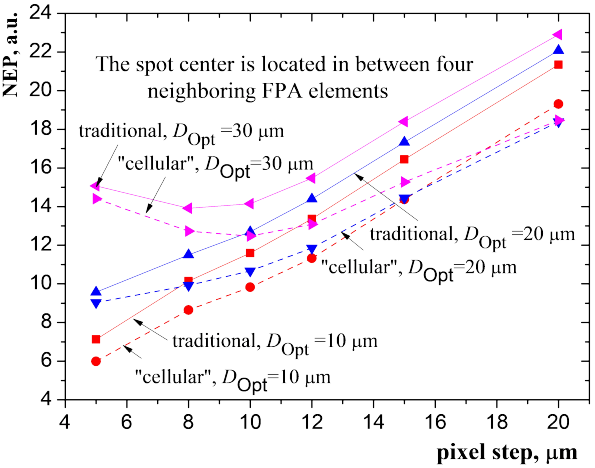

Fig. 6. The dependences of NEP on the pixel size in IR FPAs operating in BLIP mode: curves for the traditional topology; the spot center is located in between four neighboring FPA elements; for the "cellular" topology; the spot center is located at the point x

provides the best threshold sensitivity of IR FPAs (on (12 - 20)%) throughout the whole range of pixel sizes and optical-system parameters (D_{Opt} from 10 to 30 μm).

When setting a specific background radiation flux, spectral range, accumulation time, charge capacitance and level of noise Si readout circuits it is possible to calculate the real NEP IR FPA value. It is important to note the ratio for NEP on dependences the pixel size for all L_{Opt}, locations of the spot center relative to the center PE will be saved. The dependences in Figs. 5 and 6 allow one to choose an optimum pixel size consistent with the parameters of the optical system (L_{opt}).

On specifying the particular level of background radiation, the spectral range, and the integration time, from the dependences shown in Fig. 5 one can calculate the threshold sensitivity in absolute units. It should be noted here that the values quantum efficiency reported in the present work were calculated disregarding the loss of optical signals in real devices, in particular, the reflections of radiation from the non-planar surface of FPA elements, etc. However, if the IR FPA is fabricated using specific technologies, then the quantum efficiency under uniform illumination is, as a rule, known.

Note the effect due to the optical absorption length, L_{opt}, on the quantum efficiency. This effect can be diminished using a proper choice of PL stoichiometric composition making the PL long-wavelength boundary 0.3 - 0.5 μm exceeding the long-wavelength boundary of the filter used. In the latter case, the optical absorption length will be smaller than 2 - 3 μm [18]. An additional advantage of using a narrow-band filter is the suppression of the effect due to MCT-material composition inhomogeneity on decreasing fixed pattern noise [19].

For backside-illuminated scanning IR FPAs, the reflection of the substrate surfaces is a matter of primary importance. Introduction of this operation into the technological route not only ensure an increased quantum efficiency of FPA elements; it also reduces the probability of the emergence of the spurious signals due to the multiple reflections of radiation in the gap between the substrate and the internal boundary of the narrow-band filter.

4. Conclusions

The photoelectric characteristics of the traditional scanning IR FPAs containing several identical photodiode sub-arrays shifted relative to each other and feature a sparse photodiode layout were analyzed. It is shown that the photodiode layout adopted in this FPA structure requires more sophisticated manufacturing technologies of photosensitive elements, such as mesa-technology or the application of additional isolating *p-n* junctions, to be employed.

The current level of technology makes it possible to use closely spaced of photosensitive elements in linear IR FPAs fabricated using the simplest planar technology. Results of the numerical simulation of photoelectrical characteristics of linear multi-element IR FPAs with 5×5 to 20×20 μm pixel sizes used under uniform illumination and for small-sized/point objects are reported. The advantages a closely spaced configuration "shifted cellular" layout of FPA elements for scanning IR FPA in terms of the threshold sensitivity in registering small-sized point objects on 12 - 20% are demonstrated.

References

[1] PLUTON LW, 288x4 HgCdTe LWIR, the would в wide reference for 2-nd gen. scanning systems, date sheet, http://www.sofradir.com/product/pluton-lw, 2017 (accessed 20 may 2017).

[2] Sisov, F. F., Reva, V. P., Colenkov, A. G., Vasiliev, V. V. & Suslyakov, A.O. 4x288 readouts and FPAs properties. *Opto-Electron. Rev*. **14**, 76–83 (2006). http://doi.org/10.2478/s11772-006-0011-3

[3] Boltar, K. O., Burlakov, I. D. & Filachev, A. M. & Yakovleva, N.I. 6x576 FPA for the spectral range of 8-12. *Prikladnaya Fizika* **5**, 61–65 (2011).

[4] Kozlov, K. V., Patrashin, A. I., Burlakov, I. D., Bychkovsky, Y. S., Drazhnikov, B. N. & Kyznetsov, P. A. Analysis of the modern scanning infrared FPAs for remote sensing (a review). *Uspekhi prikladnoi fiziki* **5**, 63–78 (2017**).**

[5] Dvoretskii, S. A., Kochavtsev, A. P., Lee, I. I., Polovinkin, V. G., Sidorov, G. Yu. & Yakushev, M. V. Advanced Design of scanning infrared focal plane arrays. *Optoelectron. Instrum. Data Process.* **54**, 569–575 (2018). http://doi.org/10.3103/S8756699018060055

[6] Dhar, V. & Gopal, V. Optimum diode geometry in a two-dimensional photovoltaic array. *Opt. Eng*. **39**, 2022–2030 (2000). http://doi.org/10.1117/1.1.303763

[7] Vallone, M., Goano, M., Bertazzi, F., Ghione, G., Hanna, S., Eich, D. & Figgemeier, H. Diffusive-probalistic model for inter-pixel crosstalk in HgCdTe focal plane arrays. *IEEE J. Electron Devices Soc*. **6**, 662–673 (2018). http://doi.org/10.1109/JEDS.2018.2835818

[8] Fastow, R. M. & Strum, A. Monte Carlo simulations of the cross talk in InSb matrices. *Proc. SPIE* **2274**, 136–146 (1994). http://doi.org/10.1117/12.280385

[9] Juravel, Y. *et al*. The transition to second-generation HgCdTe FPA. *Proc. SPIE* **3061**, 652-661 (1997).

[10] Polovinkin, V. G., Stuchinsky, V. A., Vishnyakov, A. V. & Lee, I. I. Monte Carlo simulation of photoelectric characteristics of mercury-cadmium-tellurium based infrared-focal-plane-array detectors. *IEEE Trans. Electron Dev.* **65**, 4924–4930 (2018). http://doi.org/10.1109/TED.2018.2872129

[11] Vishnyakov A, Vasil'ev, S. I, Sidorov G. & Stuchinski V. Simulation of the charge carrier diffusion by the Monte-Carlo method for determining the spatial resolution of infrared cadmium-mercury-tellurium photodetectors. *Optoelectron. Instrum. Data Process.* **55**, 519–524 (2019). http://doi.org/10.15372/AUT20190516

[12] Polovinkin, V. G., Stuchinsky, V. A., Vishnyakov A. V. & Lee I. I. Simulation of the spatial distribution of the local quantum efficiency and photoelectric characteristics of photodiode-based infrared focal plane arrays. *Optoelectron. Instrum. Data Process.* **54**, 623–630 (2018). http://doi.org/10.3103/S8756699018060155

[13] Vasil'ev, V. V. *et al.* 320×256 HgCdTe IR FPA with a built-in shortwave cut-off filter. *Opto-Electron. Rev.* **18,** 236–240 **(**2013). http://doi.org/10.2478/s11772-010-1031-x

[14] Ivanov, V. A., Kirichuk, V. S., Kosych, V. P. & Sinel'shchikov, V. V. Specific features of detecting point objects in images formed by a detector arrays. *Optoelectron. Instrum. Data Process.* **52**, 113–120 (2016). http://doi.org/10.3103/S87566990-160-20023

[15] Goss T., Fourie H. & Viljoen J. SWIR sensor "see-spot" modelling and analysis. *Proc. SPIE* **11001,** 1100105 (2019). http://doi.org/10.1117/12.2518923

[16] Born, M. & Wolf, E. *Principles of Optics*. (Pergamon Press, 1965).

[17] Caulfield, J., Curzan, J., Lewis, J. & Dhar, N. Small pixel oversampled IR focal plane arrays. *Proc. SPIE* **9451,** 94512F-1 (2015). http://doi.org/10.1117/12.2180385

[18] Schacham, S. & Finkmanb, E. Recombination mechanisms in p-type HgCdTe: Freezeout and background flux effects. *J. Appl. Phys*. 57, 2001-2009 (1985).

[19] Mouzali, S., Lefebvre, S., Rommeluere, S., Ferrec, Y. & Primot, J. Estimation of thickness and cadmium composition distributions in HgCdTe Focal plane arrays. *J. Electron. Mater*. **45**, 4607-4611 (2016). http://doi.org/10.1007/s11664-016-4586-2